# Photoinduced Structural Changes in Fluoride Single Crystals

Yuki Toyama[1], Yasuhiko Shimotsuma[*1], Hideaki Kitahara[2], Masahiro Shimizu[1], Kiyotaka Miura[1], and Masahiko Tani[2]

[1]*Department of Material Chemistry, Kyoto University, Japan*
[2] *Research Center for Development of Far-Infrared Region, University of Fukui, Japan*
[*]*Corresponding author's e-mail: shimotsuma.yasuhiko.3m@kyoto-u.ac.jp*

Femtosecond laser pulses can induce various photoinduced structural changes inside a transparent material via nonlinear optical effects. Although solarization, caused by high-energy electromagnetic radiation, has been studied for decades and is understood as an electronic structural change caused by defect formation, the processes of defect formation and their detailed characteristics in fluoride single crystals remain unclear. Here, we clarify the mechanisms of photoinduced structural changes in fluoride single crystals. We demonstrate that femtosecond laser irradiation induces polarization-dependent birefringence in fluoride crystals. This birefringence arises from both laser-induced color center formation and the creation of nanocracks, as revealed by optical and electron microscopy. We further show that subsequent thermal annealing of the laser-processed crystals leads to precipitation of metallic nanocolloids in the irradiated regions, accounting for observed changes in optical properties. These findings provide new insights into the mechanisms of laser-induced modifications in crystalline fluoride materials and may inform the design of future photonic devices.
DOI: 10.2961/jlmn.2026.02.2002
**Keywords:** Fluoride crystal, color center, nanocolloid, femtosecond laser, birefringence

## 1. Introduction

Femtosecond lasers have been extensively used over the past decades to induce localized structural modifications inside transparent materials. Adequate laser parameters for the target materials enable the development of various photonic devices, including waveguides [1], couplers [2], optical data storage [3], micro-optics phase elements [4], integrated lab-on-chip devices [5], or fiber Bragg grating (FBG) sensors [6]. The structural modifications in crystalline materials can generally be categorized into three types: First, defect formation, such as vacancies, interstitials, and dislocations, alters the electrical and optical properties of the crystal [7]. Second, stress and lattice strain, induced by rapid thermal gradients and shock wave generation, lead to mechanical deformation and changes in physical properties [8]. Third, phase transitions or amorphization, resulting in the precipitation of metastable phases or the breakdown of long-range order, thereby modifying the material's structural and functional characteristics [9]. Unlike isotropic materials such as glass, where shockwaves propagate isotropically with respect to the optical axis of the incident laser beam, crystalline materials exhibit anisotropic shockwave propagation governed by their crystal symmetry [10]. As a result, dislocations and cracks are generated in specific directions determined by the crystallographic orientation [11]. These structural modifications, influenced by the underlying crystal structure, reflect differences in the nonlinear absorption behavior following photoexcitation, which arise from the crystal-structure-dependent anisotropy of the electron effective mass [12]. Additionally, an intriguing self-assembled nanostructure (nanograting) formation, depending on the laser polarization direction, has been observed in a glass primarily composed of network-forming oxides, such as $SiO_2$ and $GeO_2$ [13,14]. These nanogratings are attributed to the periodic distribution of oxygen-deficient and nanovoids [13], resulting in significant birefringence [3]. A characteristic feature of these nanogratings is their localized birefringence, which enables applications in five-dimensional optical data storage [3,15] and real-time polarization imaging [16]. Meanwhile, in crystalline materials, similar nanogratings have been observed in indirect-bandgap semiconductor crystals such as silicon and gallium phosphide, where the laser-induced nanogratings align parallel to the laser polarization direction [17]. These nanostructures consist of a periodically strained lattice approximately 100 nm in width.

Solarization caused by high-energy electromagnetic radiation has been studied for over 60 years and is now well understood as a change in the electronic structure resulting from defect formation [18]. In recent years, extensive research has been conducted on laser-induced color center formation in a wide range of crystalline materials. For example, the formation of color centers in YAG ceramics for laser applications [19] and the periodic distribution of color centers in fluoride crystals [20] have been reported. More recently, polarization-dependent color center formation in lithium fluoride crystals, attributed to third-order nonlinear optical phenomena, has also been demonstrated [21]. However, the processes of defect formation and detailed characteristics of these defects in fluoride single crystals remain unclear. Here, we aim to clarify the details of photoinduced structural changes within fluoride single crystals.

## 2. Experiments

### 2.1 Materials

The samples used in this experiment were fluoride single crystals of LiF (rock-salt structure), $CaF_2$, and $BaF_2$ (both fluorite structures), all 0.5 mm thick. All crystals exhibited high transparency up to the mid-infrared range, with absorption coefficients less than 1 $cm^{-1}$ extending to 6 μm for LiF, 8 μm for $CaF_2$, and 10 μm for $BaF_2$, respectively (Fig. 1).

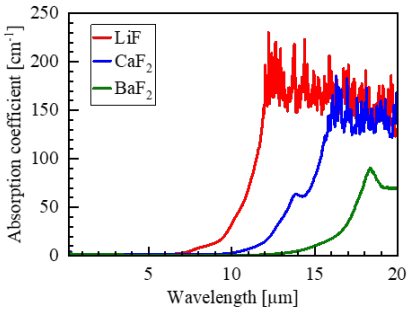


**Fig. 1** Absorption coefficient spectra for LiF, $CaF_2$, and $BaF_2$ single crystals.

### 2.2 Laser experiments

In the experiments, we used a mode-locked Ti: Sapphire laser (Coherent, λ = 800 nm, 1 kHz, 120 fs). The laser beam was focused 70 μm below the surface of fluoride single crystals in (100) face with a 50× objective lens (NA = 0.80). The pulse energy was varied from 1 μJ to 10 μJ. The scanning speed of focus was also varied from 1 μm/s to 100 μm/s. The polarization direction was tuned from 0° to 90° using a half-wave plate. This angle is defined with respect to the [100] axis, such that a 90° polarization is parallel to the [010] axis.

After laser irradiation, the focal region was inspected by an optical microscope and a polarized optical microscope. To analyze the detailed structural modification, we polished the sample surface and observed the sample surface by a field emission scanning electron microscope equipped with a focused ion beam (JEOL, JIB-4600F). We have also observed microscopic structural changes by using a transmission electron microscope (JEOL, JEM-2200FS).

### 2.3 Heat treatment

The fluoride crystal (LiF, $CaF_2$, and $BaF_2$) samples, post-femtosecond laser irradiation, were subsequently annealed in an argon atmosphere furnace (Full-Tech, FT-01VAC-30). Annealing temperatures ranged from 100 to 500°C, and heat treatment durations from 1 to 3 hours. Changes in birefringence were analyzed by observing the samples with a polarizing microscope both before and after annealing.

### 2.4 Terahertz time-domain spectroscopy (THz-TDS) measurements

To prepare a more expansive laser-treated volume within the crystal sample for terahertz time-domain spectroscopy (THz-TDS) measurements, we employed a parallelized laser processing of 14 discrete points with approximately 5 μm spacing, precisely patterned and controlled by a Liquid Crystal on Silicon Spatial Light Modulator (Hamamatsu Photonics, LCOS-SLM). Within the $CaF_2$ crystal sample, we inscribed a total of seven distinct layers (size: 8 mm × 8 mm) at varying depths by compensating for spherical aberration.

## 3. Results and discussion

### 3.1 Color center generation

To monitor the laser-induced color center formation, the localized absorption at 600 nm wavelength within the laser-processed focal volume was dynamically measured. This measurement was achieved using a home-built confocal transmission spectroscopy setup, which utilized a halogen lamp for continuous illumination and was equipped with a spectrometer (Ocean Optics, USB2000+). Spectral acquisition for each laser pulse was synchronized by a digital delay generator (Stanford Research Systems, DG535) to the laser pulse. The absorbance at 600 nm ($A$) was calculated by

$$A = 1 - \frac{1}{(1-2R)^2}\frac{I}{I_0}, \quad R = \left(\frac{1-n}{1+n}\right)^2. \qquad (1)$$

where $I_0$ and $I$ represent the incident and transmitted light intensities, respectively. $n$ denotes the refractive index of the fluoride crystal. From the refractive index at 600 nm, the sum of Fresnel reflection loss at front and back surfaces ($2R$) is calculated to be 5.3%, 6.3%, and 7.3% for LiF, $CaF_2$, and $BaF_2$, respectively.

Fig. 2 presents the evolution of localized absorption at 600 nm within the laser-processed focal volume, revealing a systematic enhancement with increasing irradiated number of pulses. This absorption change exhibited a distinct dependence on the crystal type. Indeed, a visible color change was observed in the laser-processed regions, which is attributable to the formation of F centers or their aggregated centers, such as $F_2$ centers. We also confirmed the presence of photoluminescence (PL) attributed to $F_2$ centers in the laser-processed region inside LiF crystal (data not shown).

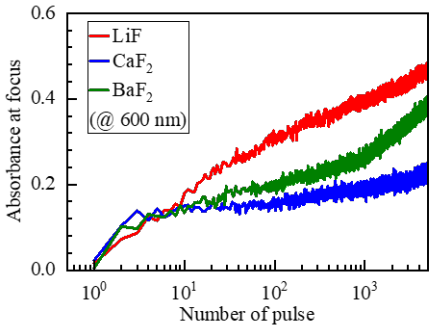


**Fig. 2** Evolution of localized absorption at 600 nm wavelength within the laser-processed focal volume as a function of the number of irradiated pulses. The laser processing parameters were 5 μJ (fixed point irradiation).

### 3.2 Polarization-dependent birefringence

Initially, these fluoride crystals lack birefringence due to their intrinsic crystal symmetry. We observed the laser-processed regions using a polarized microscope.

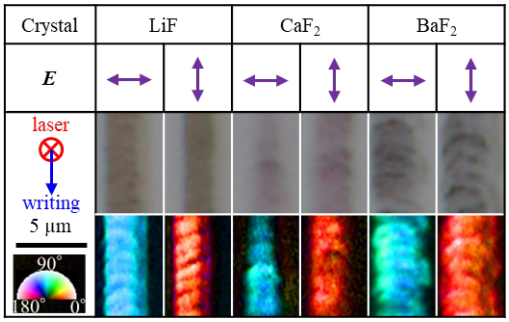


**Fig. 3** The laser-writing traces are inspected by optical (second row) and polarization (third row) microscopes. Arrows in ***E*** row denote the laser polarization direction. Pseudo color in a polarization microscope image indicates the slow axis orientation. The laser processing parameters were 1 μJ, 1 μm/s.

Fig. 3 clearly demonstrates the local photoinduction of optical anisotropy within the fluoride crystals by femtosecond laser irradiation. The slow axis of birefringence is oriented perpendicularly to the laser polarization direction. The width of the laser-processed region depended on the type of crystal. Materials with higher lattice energies require more energy to break bonds, leading to higher damage thresholds; thus, the laser-processed width varied by crystal type in a manner that correlates with their lattice energies.

Given the {100} and {111} cleavage faces for rock salt and fluorite crystal structures, respectively, we confirmed the slow axis orientation of birefringence for various laser polarization directions [Fig. 4(a)]. The measured retardation values were also crystal-dependent [Fig. 4(b)]: under laser parameters of 1 μJ and 1 μm/s, the retardation was 53 ± 9.3 nm for LiF, 30 ± 8.6 nm for $CaF_2$, and 59 ± 6.7 nm for $BaF_2$.

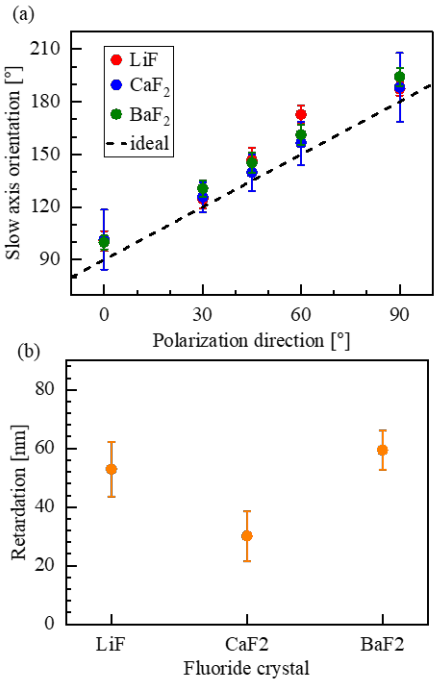


**Fig. 4** (a) Plots of photoinduced birefringence in fluoride crystals as a function of the laser polarization direction. The angle is referenced to the horizontal (zero). The dotted curve represents an ideal relationship. (b) Retardation values induced by the same laser irradiation conditions in fluoride crystals. The laser processing parameters were 1 μJ, 1 μm/s.

Table 1 summarizes key properties of various fluoride crystals, including their crystal structures, cleavage planes, defect formation energies at room temperature, surface energies for the cleavage face at room temperature, and lattice energies. Unlike the width of the laser-processed region, the magnitude of photoinduced retardation cannot be explained by lattice energy. Because the cleavage face generally possesses the lowest surface energy, it's easier to increase the interfacial area along this plane than in other orientations. This phenomenon leads to the facile formation of nanocracks along the cleavage face. The phase retardation appears to correlate with the defect formation energy and the surface energy of the cleavage face. Therefore, these results suggest that the formation of not only color centers but also nanocracks contributes to the photoinduced birefringence.

**Table 1** Properties of various fluoride crystals.

| Crystal | LiF | $CaF_2$ | $BaF_2$ |
|---|---|---|---|
| Crystal structure | Rock salt | Fluorite | Fluorite |
| Cleavage face | {100} | {111} | {111} |
| Defect formation energy [eV] | 2.14 [22] | 2.75 [23] | 1.98 [23] |
| Surface energy [$mJ/m^2$] | 340 [24] | 450 [24] | 280 [24] |
| Lattice energy [kJ/mol] | 1030 [25] | 2640 [25] | 2347 [25] |

Interestingly, despite the constraints imposed by the crystallographic orientation, the slow axis of the photoinduced birefringence is consistently aligned perpendicular to the laser polarization. For example, when a (001) surface of a LiF crystal is irradiated by laser pulses polarized along the [100] direction (0° horizontal), we anticipate nanocracks to form in the [010] direction. This is perpendicular to the polarization direction and lies along the cleavage plane. Conversely, if the polarization is at 45°, corresponding to the [110] direction, nanocracks should also be induced along the $[\bar{1}10]$ and $[1\bar{1}0]$ directions. However, their formation along these planes is expected to be more difficult due to higher surface energy. Interestingly, experimental results for the 45° polarization show that the slow axis orientation is almost perpendicular to the polarization direction [Fig. 4(a)]. Similar phenomena have also been observed in MgO crystal [26]. We interpreted that nanovoids in silica glass consistently form perpendicular to the direction of polarization. In contrast, in MgO single crystals, nanocracks form along the cleavage face, and the ratio of nanocracks formed in these two directions varies with the polarization direction.

### 3.3 Observation of photoinduced nanocracks

To investigate nanocracks formation in fluoride crystal, we dry-polished the sample surface including the laser-processed region, then prepared a small TEM specimen from this surface. Fig. 5 shows TEM observations of the $BaF_2$ crystal, including the laser-processed region.

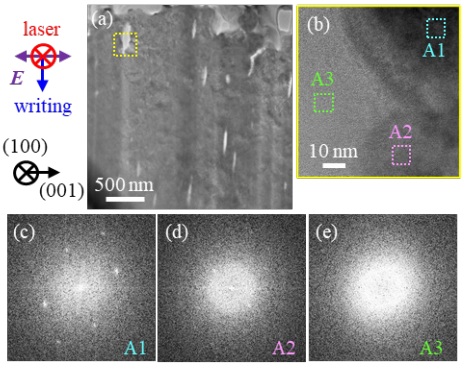


**Fig. 5** (a) TEM image of the laser-processed region in $BaF_2$ crystal. (b) Enlarged image of the yellow dotted area in (a). (c-e) FFT images of three different areas, corresponding to dotted squares of A1, A2, and A3 in (b).

The bright contrast regions, elongated in the direction perpendicular to the laser polarization, were observed. Fourier-transform images of the three typical areas highlighted in Fig. 5(b) are presented. The Fourier-transform image corresponding to dark area A1 clearly shows a pattern indicative of the existing crystal structure [Fig. 5(c)]. In contrast, no apparent pattern is observed for the bright area A3, which corresponds to the nanocracks [Fig. 5(d)]. The weak pattern observed in the A2 area [Fig. 5(e)], which surrounds the nanocracks, further indicates a reduction in crystallinity in the region adjacent to the nanovoids. These results indicate that not only color centers but also nanovoids contribute to the photoinduced birefringence. Because it is difficult to determine the laser writing direction in the sample plane during sample preparation in this experiment, further TEM observations should be performed on samples irradiated from various directions to the crystal orientation with different laser polarization directions.

### 3.4 Heat treatment of laser-processed fluoride crystals

We also investigated the fluoride crystal samples, post-femtosecond laser irradiation, which were subsequently annealed in an argon atmosphere. Fig. 6 shows PL spectra from the laser-processed region in a LiF crystal before and after heat treatment at 500°C for 3 hours. After heat treatment at 500°C for 3 hours, the PL intensity associated with the photoinduced $F_2$ centers in LiF crystal disappeared.

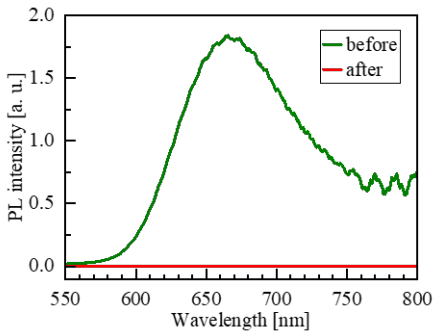


**Fig. 6** Photoluminescence spectra from the laser-processed region in a LiF crystal before and after heat treatment at 500°C for 3 hours. The laser processing parameters used were 1 μJ and 1 μm/s.

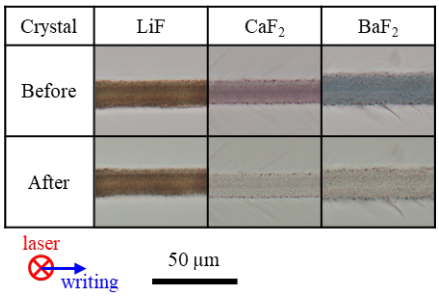


**Fig. 7** Typical optical micrographs of the laser-processed regions in fluoride crystals before (first row) and after (second row) heat treatment at 500°C for 1 hours. The laser processing parameters were 10 μJ, 10 μm/s.

Fig. 7 shows typical optical micrographs of the laser-processed regions in fluoride crystals before and after heat treatment at 500°C for 1 hours. In all crystals, the laser-processed regions exhibit visible coloring, indicating the generation of color centers. In contrast to LiF crystal, the colors of the laser-processed regions in $CaF_2$ and $BaF_2$ crystals became lighter after heat treatment. The results for LiF crystal indicate that $F_2$ centers are aggregated into complex color centers, such as $F_n$ ($n \geqq 3$) centers, during heat treatment. Table 2 lists the reported absorption bands of F and $F_2$ color centers in various fluoride crystals.

**Table 2** Reported absorption bands of F and $F_2$ color centers in fluoride crystals.

| Crystal | Color center | Band maximum | Reference |
|---|---|---|---|
| LiF | F | 250 nm | [27] |
| | $F_2$ | 445 nm | [27] |
| $CaF_2$ | F | 376 nm | [28] |
| | $F_2$ | 521 nm | [29] |
| $BaF_2$ | F | 539 nm | [30] |
| | $F_2$ | 720 nm | [31] |

Residual retardation in the laser-processed regions inside fluoride crystals after heat treatment at various temperatures for 3 hours are plotted in Fig. 8. Similar to the change in PL spectra due to $F_2$ centers (Fig. 6), in the case of LiF crystal, the photoinduced retardation of the laser-processed region decreased after heat treatment. In contrast to LiF, heat treatment leads to an increase in retardation for $CaF_2$ and $BaF_2$ crystals. This phenomenon was evident in heat treatments above 300°C. We also performed TEM observation of the $CaF_2$ crystal sample, including the laser-processed region after heat treatment at 500°C for 1 hour (Fig. 9). Nanocracks with brighter contrast elongated perpendicular to laser polarization were still observed even after heat treatment.

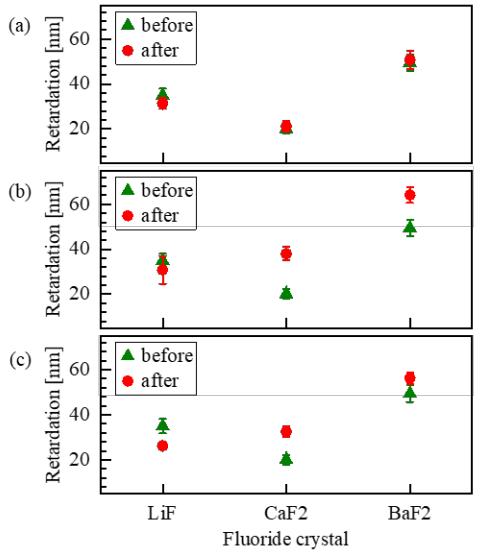


**Fig. 8** Residual retardation in the laser-processed region in fluoride crystals after heat treatment at (a) 100°C, (b) 300°C, and (c) 500°C for 3 hours. The laser processing parameters were 1 μJ and 1 μm/s.

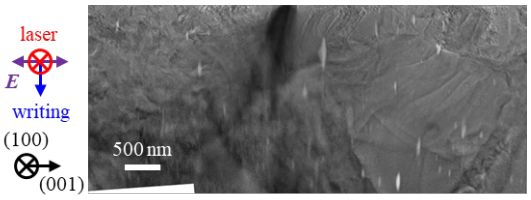


**Fig. 9** TEM image of the laser-processed region in $CaF_2$ crystal after heat treatment at 500°C for 1 hour.

### 3.5 Terahertz conductivity and nanocolloid formation

To understand the increased birefringence in $CaF_2$ and $BaF_2$ after heat treatment, we analyzed the samples using terahertz time-domain spectroscopy (THz-TDS). In this THz-TDS measurement, we used a $CaF_2$ crystal sample containing a volumetrically laser-processed region. This region consists of a group of 14 traces, with each trace approximately 1.5 µm wide and separated by a pitch of 5 µm. The laser-processed area was arranged into seven layers at different depths. The overall period of the group of 14 traces was estimated to be roughly 62 µm (Fig. 10). Based on optical microscope observations and assuming the laser tracks have approximate dimensions of 1.5 µm in width and 20 µm in height, the laser-processed volume was estimated to account for approximately 0.001% of the total sample volume.

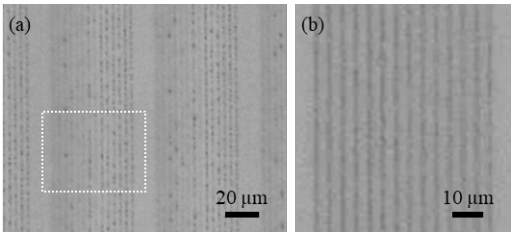


**Fig. 10** (a) Optical micrograph of the $CaF_2$ crystal sample used for THz-TDS measurements. (b) Magnified view of the dotted area shown in (a). The laser processing parameters were 0.6 µJ and 50 µm/s.

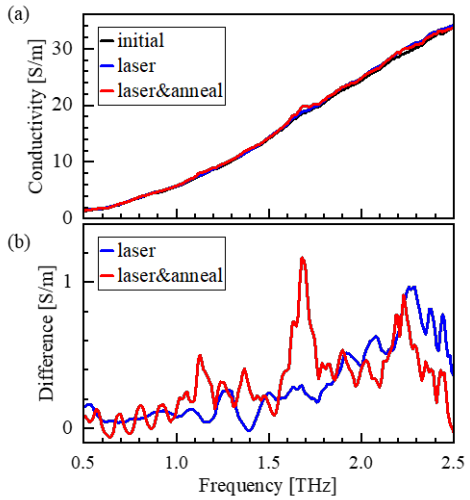


**Fig. 11** (a) Electrical conductivity as a function of the irradiated THz frequency. (b) Difference spectra between the laser-processed sample and the pristine crystal, as well as between the thermally treated laser-processed sample and the pristine crystal.

Fig. 11 shows the electrical conductivity as a function of the irradiated THz frequency. The conductivity was calculated by fitting the complex dielectric constant of the sample in the THz range using an appropriate Drude model. Since the laser-processed volume is small, the difference spectra between the laser-processed sample and the pristine crystal, as well as between the thermally treated laser-processed sample and the pristine crystal, are also presented.

The laser-processed sample after subsequent thermal treatment exhibited an increased conductivity at approximately 1.7 THz, corresponding to a wavelength of 176 µm. Assuming a refractive index of 2.62 for $CaF_2$ at a wavelength of 176 µm [32], the corresponding grating period is estimated to be approximately 67 µm. This value is in good agreement with the observed period of the group of 14 traces. These results suggest that metallic Ca nanocolloids precipitate within the laser-processed $CaF_2$ crystal upon subsequent heat treatment. Indeed, it has been reported that the dielectric constant of a $CaF_2$ crystal becomes negative after electron-beam irradiation followed by heat treatment at 500°C [33]. Consequently, the observed increase in the birefringence of $CaF_2$ and $BaF_2$ after heat treatment suggests the precipitation of metallic nanocolloids. Further studies and experiments are required to understand why this phenomenon is not observed in LiF crystals.

## 4. Conclusion

In this study, we have shown that femtosecond laser irradiation induces polarization-dependent birefringence in fluoride single crystals. This birefringence arises from both laser-induced color center formation and the creation of nanocracks, demonstrating that both electronic and structural defects contribute to optical anisotropy. We also found that thermal annealing of the laser-processed crystals (especially $CaF_2$ and $BaF_2$) leads to precipitation of metallic nanocolloids in the irradiated regions, which explains the observed increase in birefringence after heat treatment. These findings provide new insight into the mechanisms of laser-induced structural modification in crystalline fluoride materials and may inform the design of future photonic devices based on these materials.

## Acknowledgments

This work was partially supported by AMADA Foundation (AF-2023201), Amano Institute of Technology, and Research Foundation for Opto-Science and Technology. The terahertz time-domain spectroscopy experiments were performed at the Research Center for Development of Far-Infrared Region at the University of Fukui (FIR Center) (Proposal No. R05FIRDG025A and R06FIRDG022B).

## References

[1] K. M. Davis, K. Miura, N. Sugimoto, and K. Hirao: Opt. Lett., 32, (1996) 1729.
[2] N. Riesen, S. Gross, J. D. Love, and M. J. Withford: Opt. Express, 22, (2014) 29855.
[3] Y. Shimotsuma, M. Sakakura, P. G. Kazansky, M. Beresna, J. Qiu, K. Miura, and K. Hirao: Adv. Mater., 22, (2010) 4039.
[4] R. Drevinskas and P. G. Kazansky: APL Photon., 2, (2017) 066104.
[5] K. Sugioka and Y. Cheng: Lab Chip., 19, (2012) 3576.

[6] S. J. Mihailov, D. Grobnic, C. Hnatovsky, R. B. Walker, P. Lu, D. Coulas, and H. Ding: Sensors, 17, (2017) 2909.
[7] E. F. Martynovich, N. L. Lazareva, and S. A. Zilov: J. Lumin., 234, (2021) 117989.
[8] S. Kanehira, K. Miura, K. Fujita, J. Si, N. Shibata, and Y. Ikuhara: Appl. Phys. Lett., 90, (2007) 163110.
[9] M. Shimizu, Y. Shimotsuma, M. Sakakura, T. Yuasa, H. Homma, Y. Minowa, K. Tanaka, K. Miura, and K. Hirao: Opt. Express, 17, (2009) 46.
[10] M. Sakakura, T. Tochio, M. Eida, Y. Shimotsuma, S. Kanehira, M. Nishi, K. Miura, and K. Hirao: Opt. Express: 19, (2011) 17780.
[11] M. Sakakura, Y. Shimotsuma, N. Fukuda, and K. Miura: J. Appl. Phys., 118, (2015) 023106.
[12] M. Gertsvolf, H. Jean-Ruel, P. P. Rajeev, D. D. Klug, D. M. Rayner, and P. B. Corkum: Phys. Rev. Lett., 101, (2008) 243001.
[13] Y. Shimotsuma, P. G. Kazansky, J. Qiu, and K. Hirao: Phys. Rev. Lett., 91, (2003) 247405.
[14] T. Asai, Y. Shimotsuma, T. Kurita, A. Murata, S. Kubota, M. Sakakura, K. Miura, F. Brisset, B. Poumellec, and M. Lancry: J. Am. Ceram. Soc., 98, (2015) 1471.
[15] J. Zhang, M. Gecevičius, M. Beresna, and P. G. Kazansky: Phys. Rev. Lett., 112, (2014) 033901.
[16] T. Ohfuchi, M. Sakakura, Y. Yamada, N. Fukuda, T. Takiya, Y. Shimotsuma, and K. Miura: Opt. Express, 25, (2017) 23738.
[17] M. Mori, Y. Shimotsuma, T. Sei, M. Sakakura, K. Miura, and H. Udono: Phys. Status Solidi A, 212, (2015) 715.
[18] R. B. Gordon: Am. Sci., 47, (1959) 361.
[19] L. Zhang, J. Wu, P. Stepanov, M. Haseman, T. Zhou, D. Winarski, P. Saadatkia, S. Agarwal, F. A. Selim, H. Yang, Q. Zhang, Y. Wang, C. Wong, and H. Chen: Photon. Res., 7, (2019) 549.
[20] L. Bryukvina: J. Lumin., 162, (2015) 145.
[21] E. F. Martynovich, V. P. Dresvyansky, A. L. Rakevich, N. L. Lazareva, M. A. Arsentieva, A. A. Tyutrin, O. Bukhtsoozh, S. Enkhbat, P. V. Kostryukov, B. E. Perminov, and A. V. Konyashchenko: Appl. Phys. Lett., 114, (2019) 121901.
[22] M. Lazaridou, C. Varotsos, K. Alexopoulos, and P. Varotsos: J. Phys. C: Solid State Phys., 18, (1985) 3891.
[23] C. R. A. Catlow, M. J. Norgett, and T. A. Ross: J. Phys. C: Solid State Phys., 10, (1977) 1627.
[24] J. J. Gilman: J. Appl. Phys., 31, (1960) 2208.
[25] "Handbook of Chemistry and Physics 96th ed." ed. by W. M. Haynes (CRC Press, London, 2015) p.1221.
[26] T. Sakurai, Y. Shimotsuma, M. Shimizu, and K. Miura: J. Laser Micro Nanoeng., 19, (2024) 51.
[27] K. Schwartz, A. E. Volkov, M. V. Sorokin, R. Neumann, and C. Trautmann: Phys. Rev. B, 82, (2010) 144116.
[28] B. C. Cavenett, W. Hayes, I. C. Hunter, and A. M. Stoneham: Proc. R. Soc. Lond. A, 309, (1969) 53.
[29] "Crystals with the fluorite structure" ed. by W. Hayes (Oxford University Press, London 1974) p.448.
[30] A. I. Nepomnyashchikh, E. A. Radzhabov, A. V. Egranov, V. F. Ivashechkin, and A. S. Istomin: Radiat. Eff. Defects Solids, 157, (2002) 715.
[31] P. K. Chakraborty and K. V. Rao: J. Mater. Sci., 22, (1987) 587.
[32] D. R. Bosomworth: Phys. Rev., 157, (1967) 709.
[33] F. Beuneu and P. Vajda: J. Appl. Phys., 78, (1995) 6989.

(Received: June 30, 2025, Accepted: March 1, 2026)